The Astrophysical Journal, 970:144 (13pp), 2024 August 1 https://doi.org/10.3847/1538-4357/ad517e

Cosmic-Ray Transport in the Presence of a Fisk-type Heliospheric Magnetic Field: Investigating the Influence of Drift

J. S. Troskie[1,2], N. E. Engelbrecht[1], and P. J. Steyn[1]
[1] Centre for Space Research North-West University Potchefstroom, 2522, South Africa; jst99960@gmail.com
[2] South African National Space Agency Hermanus, 7200, South Africa
Received 2024 March 12; revised 2024 May 7; accepted 2024 May 27; published 2024 July 26

Abstract

Drifts due to the gradients in, and curvatures of, the heliospheric magnetic field (HMF) play a significant role in the transport of galactic cosmic rays (GCRs) in the heliosphere. Although this has been well studied for the Parker HMF, the influence of Fisk-type fields, with their unique geometry, has hitherto received less attention. Here, drift velocity profiles computed for a Schwadron–Parker hybrid field are compared with those for a purely Parkerian field. Furthermore, the influence of this field on GCR modulation, as computed with a 3D, ab initio, modulation model, is investigated. Globally, the differences between the computed intensities are small. Nevertheless, local measures, such as azimuthal variations in the GCR intensities, show a significant influence of the Schwadron–Parker hybrid field on GCR transport.

Unified Astronomy Thesaurus concepts: Galactic cosmic rays (567); Heliosphere (711); Interplanetary turbulence (830)

1. Introduction

The large-scale structure of the heliospheric magnetic field (HMF) is often approximated using the comparatively simple model proposed by Parker (1958), in which field lines are assumed to form Archimedean spirals around the rotation axis of the Sun. In this model, the HMF consists of a radial and an azimuthal component, and does not vary azimuthally, except at the wavy heliospheric current sheet (HCS), across which a polarity change occurs. Furthermore, the solar wind speed is assumed to be constant in the original Parker model (however, see, e.g., the modified field of Burger & Sello 2005), although a latitude-dependent solar wind speed is sometimes employed (e.g., Hitge & Burger 2010). While observations have long suggested that the large-scale structure of the HMF is generally well approximated by the Parker model, especially near the ecliptic plane (see, e.g., Neugebauer 1976; Ness & Burlaga 2001), Ulysses Fast Latitude Scan (see Wenzel et al. 1990; Wenzel 1995) observations of high-latitude 26 days variations in galactic cosmic-ray (GCR) proton intensities in both the northern and southern hemispheres of the heliosphere (see, e.g., Simpson et al. 1995b; Paizis et al. 1999) provided some motivation to revisit the standard Parker model. This was because the corotating interaction regions whence these variations originate (see, e.g., Kóta & Jokipii 1998 and references therein) simply did not persist to high enough latitudes (Gosling & Pizzo 1999) to explain this phenomenon, which also could not be attributed to HCS drift effects, due to the relatively low tilt angles observed during solar minima. Furthermore, the observed GCR latitude gradients were also reported to be significantly lower than expected from prior modulation studies assuming a standard Parker field (Simpson et al. 1995a; Heber et al. 1996, 2008), with larger latitude gradients reported during periods of positive magnetic polarity ($A > 0$) than during periods of negative ($A < 0$) polarity (de Simone et al. 2011; Gieseler & Heber 2016). It later became apparent that the recurrent variations and latitude gradients were related (Zhang 1997; Paizis et al. 1999), with Zhang (1997) reporting a linear relationship between the amplitudes of these variations and the latitude gradients of GCR protons. The apparent interconnectedness of these phenomena implied the existence of an additional mechanism whereby GCR particles could be latitudinally transported, which an HMF model with a significant meridional component, lacking in the Parker model, could in principle provide.

Fisk (1996) introduced an HMF model to provide an explanation for the abovementioned recurrent energetic particle events observed at high latitudes by the Ulysses spacecraft. The rotational axis $\boldsymbol{\Omega}$ is assumed to be separated from the magnetic axis $\boldsymbol{M}$ by a tilt angle α. The $\hat{p}$-axis is defined by a magnetic field line originating from the solar pole (no differential rotation assumed here) and is separated from the rotational axis by an angle β, commonly referred to as the Fisk angle. Fisk-type field lines are assumed to originate from rigidly rotating polar coronal holes (PCHs) and expand from the photosphere to the solar wind source surface (SWSS) symmetrically about $\boldsymbol{M}$. The differential rotation ω of the field line footpoints on the photosphere and the super-radial expansion of field lines to the SWSS cause the Fisk model to display large excursions in heliographic latitude. The expansions of the field lines form footpoint trajectories on the SWSS symmetrically about the $\hat{p}$-axis.

Several modifications and generalizations of the Fisk HMF have been suggested in the past. For example, magnetic field observations from the Ulysses spacecraft reported underwound magnetic field lines, which prompted Schwadron (2002) to introduce a generalization of the Fisk field. The underwound field was correlated with the frequency of corotating rarefaction regions and showed that the phenomenon is likely influenced by two factors, namely the motion of footpoints of open magnetic field lines on the Sun from crossing coronal hole boundaries and the effect of solar wind shearing in rarefaction regions. Taking this into account, the Schwadron model was

further generalized to include a latitude-dependent solar wind speed (Schwadron & McComas 2003).

Burger & Hitge (2004) introduced a Fisk–Parker hybrid field, where a standard Parker field is assumed in the ecliptic plane and changes to a more Fisk-type field with decreasing colatitude toward the solar pole. The change from Parker to Fisk-type behavior is done by the use of a transition function F_s, where β and ω scale with F_s in order for both arguments to become zero when the field is Parker-like in the ecliptic. Burger et al. (2008) refined the Fisk–Parker model, which is easier to implement in numerical modulation models than a pure Fisk field, but is still a reasonable approximation for the case when field lines open into the heliosphere, both in the PCHs and at low latitudes. Note that these Fisk–Parker hybrid fields are derived assuming a constant solar wind speed. Subsequently, Hitge & Burger (2010) proposed a similar hybrid field, but now taking into account the observed latitude dependence of the solar wind speed during solar minimum, by employing the abovementioned Schwadron field. Once more, this was done by employing the latitude-dependent transition function of Burger et al. (2008).

Steyn & Burger (2020) present a generalization of the Fisk field, by relaxing the assumption that the differential rotation rate is a constant fraction of the equatorial rotation rate (typically $\Omega/4$). Rather, they implement the observed spatially dependent differential rotation rate of the photosphere as reported by Snodgrass (1983). Dealing with the differential rotation in this way removes the need for a transition function F_s used by Burger et al. (2008), since now the magnetic field behavior changes naturally from a Parker field in the equatorial region to a Fisk-type field in the off-ecliptic region. Comparing the predicted and observed winding angles from in situ magnetic field measurements from the Ulysses mission, Steyn & Burger (2020) show that the generalized Fisk field compares better overall with the observed magnetic field data than the standard Parker and Schwadron field models. However, since this model assumes a latitudinal dependence in the differential rotation rate, it presents challenges for use in the current study. Furthermore, it can be seen from Steyn & Burger (2020) that the geometry of this field is very similar to that of the Schwadron–Parker (SP) hybrid field proposed by Hitge & Burger (2010). Therefore, in what follows, this study employs an SP hybrid field with a latitudinal solar wind dependence.

It should be noted that direct observational evidence for Fisk-type fields has thus far been rather limited and ambiguous. While some studies report on evidence for such fields from analyses of Ulysses spacecraft observations of the HMF (Zurbuchen et al. 1997), others find no evidence of such a field (Roberts et al. 2007). Forsyth et al. (2002), in their analysis, also do not find direct evidence for a Fisk-type field, but point out that the amplitudes of the deviations of the observations from what is expected of a Parker field could be too low to detect with the available data and therefore cannot rule out the presence of such a field, a point further discussed by Burger et al. (2008) and originally raised by Fisk (2001). Intriguingly, the 3D time-dependent magnetohydrodynamic HMF simulations of Lionello et al. (2006) support the possible existence of an HMF with field lines undergoing latitudinal excursions, like the Fisk-type field models. More recently, Steyn et al. (2024) have investigated magnetic field measurements from the Wind and ACE spacecraft to investigate the coronal sources of L1 solar wind disturbances during three solar minima epochs, using the Fisk HMF and comparing them with a standard Parker field tracing and potential field extrapolations. When the Fisk HMF geometry is assumed, 88% of magnetic field tracings successfully connect solar wind disturbances observed at L1 to PCHs (which are believed to be the origins of Fisk-type fields). The locations of the PCHs were also confirmed in that study by investigating the observed O^{7+}/O^{6+} ratios. As such, several studies have attempted to glean indirect evidence for such fields by way of cosmic-ray (CR) modulation and transport studies in the presence of these fields. Several studies have demonstrated that Fisk-type fields can in principle reproduce both the reduced-latitude gradients and high-latitude recurrent-intensity variations of GCR protons, as well as the reported relationship between these two quantities, for various Fisk-type HMF models (Burger & Hitge 2004; Burger et al. 2008; Hitge & Burger 2010) as well as for GCR electrons (Engelbrecht & Burger 2010). Furthermore, Sternal et al. (2011) modeled the transport of Jovian electrons in the presence of a Fisk-type field and reported that such a field could also explain the recurrent high-latitude variations of these low-energy particles. However, after a direct comparison with Ulysses observations, these authors report that the amplitudes of these variations could only be reproduced by assuming a greatly reduced Fisk effect (a finding in agreement with what was concluded by, e.g., Forsyth et al. 2002). These studies primarily concerned themselves with the influence of Fisk-type fields on the diffusion of GCRs, and to date the influence of the unique geometry of such fields on particle drifts has not been considered in great detail. This is one of the aims of the present study.

It should, however, be noted that enhanced latitudinal transport due to the presence of HMF field lines with significant meridional components is not the sole mechanism that has been proposed to explain reduced GCR latitude gradients. The higher levels of turbulence observed at high latitudes in the fast solar wind (Jokipii et al. 1995; Bavassano et al. 2000a, 2000b; Erdős & Balogh 2005) can in principle lead to higher levels of perpendicular diffusion at these latitudes relative to the ecliptic plane, by simply enhancing the perpendicular diffusion coefficient, whether in the radial or meridional direction. It was demonstrated by Engelbrecht & Burger (2013), via careful turbulence transport modeling of the relevant turbulence quantities, that such a meridional enhancement of the isotropic perpendicular diffusion coefficient can lead to a reduction of the computed GCR proton latitude gradients to such a degree that these are in reasonable agreement with spacecraft observations (see also Shen et al. 2021). This agreement, however, only extends to latitude gradients during periods of positive magnetic polarity, not negative polarity. It should be noted that Moloto et al. (2019), using a similar model, also showed that such a model cannot reproduce the longitudinal GCR intensity variations observed by Ulysses, due to the lack of azimuthal variations in the transport coefficients. Furthermore, studies invoking anisotropic perpendicular diffusion, where the meridional perpendicular diffusion coefficient is enhanced in some way relative to the radial perpendicular diffusion coefficient (see, e.g., Jokipii 1973; Jokipii et al. 1995), have been able to reproduce the observed reduced-latitude gradients while employing a purely Parkerian HMF model (see, e.g., Burger et al. 2000) for both $A > 0$ and $A < 0$. However, the exact enhancement factor often varies between such studies, seemingly chosen so as to

achieve agreement with spacecraft data, and it is to be understood that such an approach also cannot reproduce the observed high-latitude azimuthal variations in GCR intensities (see the discussion in Moloto et al. 2019).

The present study also aims to fully incorporate drift effects due to a Fisk-type field, namely the SP HMF proposed by Hitge & Burger (2010), into the ab initio GCR modulation model of Engelbrecht & Burger (2015a), in order to study the influence of such drift effects on computed GCR proton intensities and latitude gradients, while also modeling GCR diffusion and drift, and the turbulence quantities these processes depend on, in as self-consistent a manner as possible. The following section is devoted to an in-depth comparative study of the drifts due to a standard Parker field as well as the drifts due to an SP field. The section following that will investigate the influence of these effects on computed GCR intensities and latitude gradients. The paper closes with a section devoted to a discussion of the results so acquired.

2. GCR Drifts in the Presence of a SP Hybrid Field

Given a nearly isotropic distribution of CRs and an HMF given by $\vec{B}$ (which, in the present context, may be a Parker or a Fisk-type field), the average drift velocity of the particle distribution may be calculated from the expression given by Isenberg & Jokipii (1979):

$$\vec{v}_d = \nabla \times \kappa_A \hat{e}_B. \tag{1}$$

In the expression above, $\hat{e}_B$ denotes a unit vector in the local direction of the HMF, and the drift coefficient κ_A is given, for the weak-scattering case, by Forman et al. (1974):

$$\kappa_A = \frac{v}{3} R_L = \frac{p v_\perp}{3qB} = \frac{\beta P}{3B}, \tag{2}$$

where $v_\perp$ is the speed of the particle perpendicular to the HMF, p is the magnitude of the momentum of the particle, q is the charge magnitude, and the (maximal) Larmor radius is given by $R_L = \gamma m v_\perp/(qB)$, where m is the particle rest mass and γ is the Lorentz factor. Alternatively, κ_A may be written in terms of P, the particle rigidity, and the ratio v/c, denoted by β. It is to be noted that the drift coefficient given by Equation (2) is only valid in the weak-scattering limit, when the influence of HMF turbulence on particle drift is negligible (see, e.g., Engelbrecht et al. 2022 and references therein).

Furthermore, note that Equation (3) is undefined where $B = 0$. Therefore, it cannot be applied at the HCS. In order to model the drift due to the HCS, a number of models may be employed. These include the models of Burger (2012) and Engelbrecht et al. (2019), the latter of which is applied in the present study (see also the model of Burger et al. 1985 and the related discussions in Strauss et al. 2012 and Mohlolo et al. 2022). Following Burger (2012), Engelbrecht et al. (2019) modify the drift coefficient by using a transition function, so chosen in order to approximate the Heaviside step function, where $\kappa_A \rightarrow f(\delta)\kappa_A$, such that

$$\vec{v}_d = f(\delta)\nabla \times (\kappa_A \hat{e}_B) - \kappa_A \hat{e}_B \times \nabla f(\delta), \tag{3}$$

where the first term models the HCS drift and the second the drift due to the gradients in, and curvatures of, the particular HMF model under consideration. Note that the sign of the unit vector $\hat{e}_B$ written in Equation (3) is determined by the polarity of the HMF in the northern hemisphere, with the polarity inversion across the HCS now being taken into account by the modified drift coefficient $f(\delta)\kappa_A$. The transition function is given by $f(\delta) = 2S(\delta) - 1$, where S is a higher-order smoothstep (e.g., Ebert et al. 2002) function:

$$S(\delta) = \begin{cases} 0 & \text{if } \delta < 0; \\ 924\delta^{13} - 6006\delta^{12} + 16380\delta^{11} & \\ -24024\delta^{10} + 20020\delta^{9} - 9009\delta^{8} + 1716\delta^{7} & \text{if } 0 \leqslant \delta \leqslant 1; \\ 1 & \text{if } \delta > 1, \end{cases} \tag{4}$$

with $S'(\delta) = S''(\delta) = 0$ if $\delta \leqslant 0$ or $\delta \geqslant 1$. Because the smoothstep function and its derivatives are clamped, no artificial terms (see the third term of $\vec{v}_d$ as presented by Burger 2012) arise due to the application of the chain rule in calculating the drift velocity (Equation (3)), which have been shown to influence the transport of GCRs (Kopp et al. 2017). The quantity δ is defined as

$$\delta = \frac{1}{2} + \frac{r(\theta_{ns} - \theta)}{4R_L}, \tag{5}$$

where θ_{ns} is the latitudinal extent of the HCS, here modeled using (Kóta & Jokipii 1983)

$$\theta_{ns} = \frac{\pi}{2} - \tan^{-1}\left[\tan\alpha \sin\left(\frac{\Omega r}{V_{SW}}\right)\right], \tag{6}$$

where Ω denotes the solar rotation rate, V_{SW} the solar wind speed, and α the heliospheric tilt angle, chosen here to be equal to 10° in order to simulate generic solar minimum conditions. Note that the second term on the right-hand side of Equation (5) for δ above is larger by a factor of 2 than the term given by Engelbrecht et al. (2019), due to a typo in that paper. Due to the manner in which δ is defined, the drift effects arising from the HCS will only affect CRs within a distance $2R_L$ above and below the HCS. Finally, note that the quantity δ, being defined in terms of the Larmor radius, naturally results in an energy dependence for HCS drift effects.

In order to calculate the drift velocity due to the gradient and curvature drifts, the second term in Equation (3) needs to be evaluated with a unit vector $\hat{e}_B$ appropriate to the HMF model under consideration. For a Parker field, this quantity can rather simply be expressed in terms of the winding angle Ψ as $\hat{e}_B = \cos\Psi\hat{e}_r - \sin\Psi\hat{e}_\phi$ (see, e.g., Burger 2012). In what is to follow, $\hat{e}_B$ will be calculated directly by dividing the vector field by its magnitude, such that $\hat{e}_B = \vec{B}/B$. The SP hybrid field is employed in what is to follow, given by (Hitge & Burger 2010)

$$\begin{aligned} B_r &= A\left(\frac{r_0}{r}\right)^2\left(1 + \frac{r}{V_{SW}^2}\omega^* \sin\beta^* \sin\phi^* \frac{\partial V_{SW}}{\partial\theta}\right) \\ B_\theta &= \frac{A r_0^2}{r V_{SW}}\omega^* \sin\beta^* \sin\phi^* \\ B_\phi &= \frac{A r_0^2}{r V_{SW}}\Big[\omega^* \cos\beta^* \sin\theta + \frac{d}{d\theta} \\ &\quad \times (\omega^* \sin\beta^* \sin\theta)\cos\phi^* - \Omega\sin\theta\Big], \end{aligned} \tag{7}$$

with the differential rotation rate $\omega^* = \omega F_S$ and Fisk angle $\beta^* = \beta F_S$ written in terms of a latitude-dependent transition function, given by

$$F_S = \begin{cases} \{\tanh[\delta_p\theta] + \tanh[\delta_p(\theta-\pi)] - \tanh[\delta_e(\theta-\theta'_b)]\}^4 & \text{if}\theta \in [0,\ \theta'_b); \\ 0 & \text{if}\theta \in [\theta'_b,\ \pi-\theta'_b]; \\ \{\tanh[\delta_p\theta] + \tanh[\delta_p(\theta-\pi)] - \tanh[\delta_e(\theta-\pi-\theta'_b)]\}^4 & \text{if}\theta \in (\pi-\theta'_b,\ \pi]. \end{cases} \quad (8)$$

Here, $\delta_p = 5.0 = \delta_e$ are constants affecting the gradients of F_S, their values being chosen so as to coincide with those of Burger et al. (2008) and Sternal et al. (2011), and $\theta'_b = 80°$. The transition function is solely a function of colatitude, to ensure a divergence-free HMF (Burger & Hitge 2004; Steyn & Burger 2020). At colatitudes close to the ecliptic plane, and directly over the poles, $F_S = 0$ and the resulting HMF is Parkerian. At intermediate colatitudes, $0 < F_S \leqslant 1$, and the field is more Schwadron (2002)–like. The Fisk angle is here modeled following, e.g., Burger et al. (2008), such that

$$\beta = \arccos\left[1 - (1 - \cos\theta^{ss}_{mm})\left(\frac{\sin^2\alpha}{\sin^2\theta^{ph}_{mm}}\right)\right] - \alpha, \quad (9)$$

where θ^{ss}_{mm} denotes the maximum expansion boundary in heliographic colatitude on the SWSS of the HMF lines originating from the modeled PCH, and θ^{ph}_{mm} denotes the photospheric heliomagnetic colatitude of said PCH boundary. These quantities are here modeled following Burger et al. (2008). The latitude dependence of the solar wind velocity is modeled using a standard hyperbolic tangent function, such as that employed by, e.g., Ferreira et al. (2001) and Hitge & Burger (2010), and given by

$$V_{SW} = 400\ \text{km}\cdot\text{s}^{-1} \times \begin{cases} 1.5 - 0.5\tanh[8(\theta - \pi/2 + \alpha + \varphi_t)] & \text{if} \quad \theta \leqslant \pi/2; \\ 1.5 + 0.5\tanh[8(\theta - \pi/2 - \alpha - \varphi_t)] & \text{if} \quad \theta > \pi/2, \end{cases} \quad (10)$$

with $\varphi_t = 15°$, which reproduces the observed latitudinal dependence of this quantity (Phillips et al. 1995; McComas et al. 2000).

The reducing influence of turbulence on the drift coefficient, particularly at higher latitudes, where greater turbulence levels have been reported, is expected to reduce any signature of a Fisk-type field in GCR drift velocities and is taken into account here by using the expression for the turbulence-reduced drift coefficient derived by Engelbrecht et al. (2017), such that

$$\kappa_A = \frac{vR_L}{3}\left[1 + \frac{\lambda^2_\perp}{R^2_L}\frac{\delta B^2_T}{B^2_0}\right]^{-1} = \frac{v\lambda_A}{3}, \quad (11)$$

where $\delta B^2_T = B^2_{2D} + B^2_{sl}$ denotes the total (slab+2D) magnetic variance, and λ_A is a length scale associated with the above diffusion coefficient, defined in the same way as a mean free path (MFP; Shalchi 2009). The reduction factor above now also depends on the GCR parallel and perpendicular MFPs. These quantities are modeled using the same expressions employed by, e.g., Burger et al. (2008), Moloto et al. (2018, 2019), Engelbrecht & Wolmarans (2020), and Engelbrecht & Moloto (2021), which have been shown to yield GCR intensities in reasonable to good agreement with spacecraft observations for both GCR protons and antiprotons, and are well described in the cited studies. The parallel MFP expression is derived from magnetostatic quasilinear theory (see, e.g., Jokipii 1966; Shalchi et al. 2004) and is given by Teufel & Schlickeiser (2003):

$$\lambda_\parallel = \frac{3s}{(s-1)}\frac{R^2}{k_{\min}}\frac{B^2_0}{\delta B^2_{sl}}\left[\frac{1}{4\pi} + \frac{2R^{-s}}{\pi(2-s)(4-s)}\right], \quad (12)$$

with $s = 5/3$ being the inertial range spectral index, $k_{\min}$ the wavenumber at which the inertial range commences, δB^2_{sl} the total slab magnetic variance, and $R = R_L k_{\min}$. Note that the above expression implicitly assumes a slab spectral form with a wavenumber-independent energy-containing range and a Kolmogorov inertial range. The perpendicular MFP is derived from the nonlinear guiding center theory (Matthaeus et al. 2003), now assuming a similar 2D turbulence spectral form as was the case for the parallel MFP with a wavenumber-independent energy range and a Kolmogorov inertial range, given by (Shalchi et al. 2004; Burger et al. 2008)

$$\lambda_\perp = \left[\alpha^2\sqrt{3\pi}\frac{2\nu-1}{\nu}\frac{\Gamma(\nu)}{\Gamma(\nu-1/2)}\lambda_{2D}\frac{\delta B^2_{2D}}{B^2_0}\right]^{2/3}\lambda^{1/3}_\parallel, \quad (13)$$

where the subscript "2D" denotes 2D turbulence quantities, $\nu = 5/6$ has the Kolmogorov (see, e.g., Burger et al. 2022) inertial range spectral index, and $\alpha^2 = 1/3$ is a parameter related to the tendency of particles to follow magnetic field lines, chosen to be the value reported by Matthaeus et al. (2003) from numerical test-particle simulations. These diffusion and drift coefficients enter into the diffusion tensor in the Parker (1965) CR transport equation (see Section 3), given in spherical coordinates by (Burger et al. 2008)

$$\begin{aligned} \kappa_{rr} &= (\kappa_\parallel\cos^2\psi + \kappa_{\perp,3}\sin^2\psi)\cos^2\zeta + \kappa_{\perp,2}\sin^2\zeta \\ \kappa_{r\theta} &= (\kappa_\parallel\cos^2\psi + \kappa_{\perp,3}\sin^2\psi - \kappa_{\perp,2})\sin\zeta\cos\zeta - \kappa_A\sin\psi \\ \kappa_{r\phi} &= (-\kappa_\parallel + \kappa_{\perp,3})\sin\psi\cos\psi\cos\zeta - \kappa_A\cos\psi\sin\zeta \\ \kappa_{\theta r} &= (\kappa_\parallel\cos^2\psi + \kappa_{\perp,3}\sin^2\psi - \kappa_{\perp,2})\sin\zeta\cos\zeta + \kappa_A\sin\psi \\ \kappa_{\theta\theta} &= (\kappa_\parallel\cos^2\psi + \kappa_{\perp,3}\sin^2\psi)\sin^2\zeta + \kappa_{\perp,2}\cos^2\zeta \\ \kappa_{\theta\phi} &= (-\kappa_\parallel + \kappa_{\perp,3})\sin\psi\cos\psi\sin\zeta + \kappa_A\cos\psi\cos\zeta \\ \kappa_{\phi r} &= (-\kappa_\parallel + \kappa_{\perp,3})\sin\psi\cos\psi\cos\zeta + \kappa_A\cos\psi\sin\zeta \\ \kappa_{\phi\theta} &= (-\kappa_\parallel + \kappa_{\perp,3})\sin\psi\cos\psi\sin\zeta - \kappa_A\cos\psi\cos\zeta \\ \kappa_{\phi\phi} &= \kappa_\parallel\sin^2\psi + \kappa_{\perp,3}\cos^2\psi, \end{aligned} \quad (14)$$

where the different angles in the above are given by

$$\tan\psi = -\frac{B_\phi}{\sqrt{B^2_r + B^2_\theta}}, \qquad \tan\zeta = \frac{B_\theta}{B_r}, \quad (15)$$

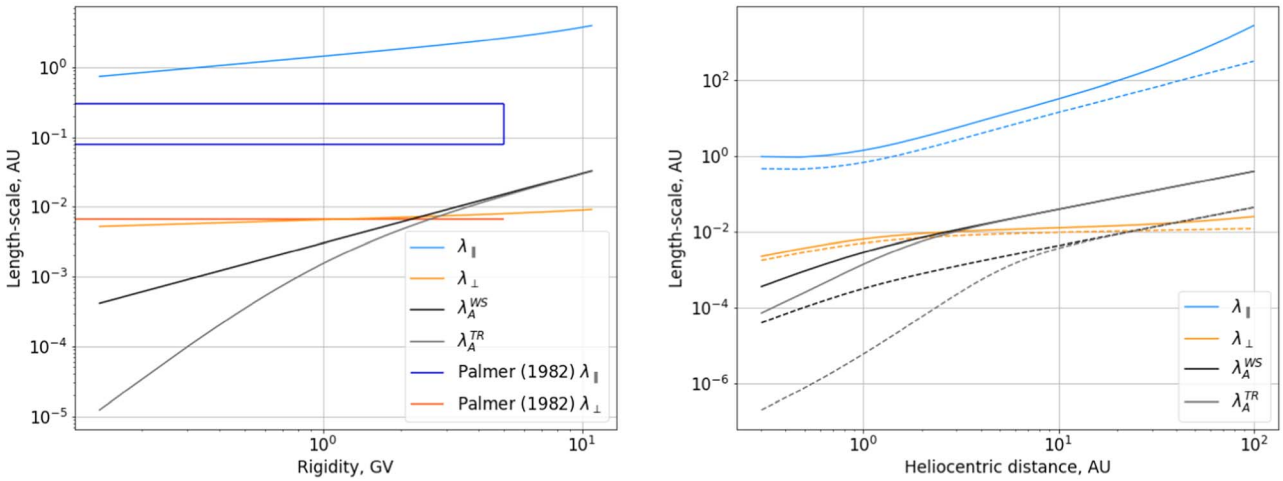

Figure 1. The MFPs, Larmor radii, and turbulence-reduced drift scales used in this study, as a function of rigidity at 1 au along with Palmer (1982) consensus-range values (left panel) and as a function of radial distance in the ecliptic plane at 0.1 GV (dashed lines) and 1 GV (solid lines) in the right panel. See the text for details.

with ψ being the winding angle for a 3D HMF such as the SP field (Equation (7)). From the above, it is evident that the use of such a HMF will drastically influence the transport of CRs, due to the latitudinal excursions of the SP HMF lines. Should a field without a meridional component, such as a Parker HMF, be employed, the above expression reduces to that presented by, e.g., Kobylinski (2001), with a more standard definition of the HMF winding angle (see, e.g., Smith & Bieber 1991).

The basic turbulence quantities, such as magnetic variances, needed to calculate the diffusion coefficients as well as the turbulence-reduced drift coefficient are here calculated as in Engelbrecht & Burger (2015a, 2015b)—that is to say, using outputs from the two-component Oughton et al. (2011) turbulence transport model. Although this code employs the same inner boundary values as proposed by Engelbrecht & Burger (2013), which were chosen so that the model outputs were in agreement with higher-latitude Ulysses turbulence observations, the contribution of pickup-ion-generated turbulence is ignored. This is due to the fact that such turbulent fluctuations occur at large frequencies (see, e.g., Williams & Zank 1994) and thus are not expected to influence the transport of GCR protons at the energies of interest to this study (Engelbrecht 2017). For more information on turbulence transport models, the interested reader is invited to consult Adhikari et al. (2021) and Oughton & Engelbrecht (2021). As this turbulence transport model is restricted to modeling the evolution of transverse turbulence quantities, and thus cannot model the mostly compressive turbulence in the heliosheath (see, e.g., Fraternale et al. 2022 and references therein), the present model assumes a boundary at 100 au.

In Figure 1, the length scales used in the calculation of the turbulence-reduced drift coefficient (Equation (11)) are shown both as a function of rigidity (left panel) and heliocentric distance (right panel). The quantities shown include the parallel and perpendicular MFPs, indicated respectively by the blue and orange lines, as well as the drift scale, computed in both the weak-scattering limit and with the drift reduction due to turbulence taken into account. The weak-scattering drift scale λ_A^{WS} is represented by a black line, while the turbulence-reduced drift scale λ_A^{TR} is represented by a gray line. In the left panel, a heliocentric distance of 1 au has been assumed. Here, the MFP consensus values reported by Palmer (1982) are also shown; for $\lambda_\parallel$, the consensus range is indicated by a blue rectangle, ranging from 0.08 to 0.3 au across the rigidity domain $0.0005\text{GV} \leqslant P \leqslant 5\text{GV}$. The Palmer (1982) consensus value for $\lambda_\perp$ is also shown, as a horizontal orange line (at $\sim$0.0067 au) intersecting the perpendicular MFP at approximately 1 GV. In the right panel, the variation of the aforementioned length scales with heliocentric distance is shown. The solid lines represent such quantities computed for a proton rigidity of 1 GV, while the length scales calculated for $P = 0.1$ GV are indicated by dashed lines.

For the rigidity-dependent variation of the aforementioned length scales (the left panel of Figure 1), increases with P are seen for the quantities $\lambda_\parallel$, $\lambda_\perp$, and λ_A (computed both in the weak-scattering limit and with drift reduction due to turbulence taken into account). The values for $\lambda_\parallel$ shown here remain above the Palmer (1982) consensus values, consistent with the solar minimum conditions assumed in the present study (e.g., Moloto et al. 2018). Furthermore, it is noted that λ_A^{TR} approaches the drift scale computed in the weak-scattering limit at high proton rigidities. As expected, the diminishing effect of turbulence on particle drift is most pronounced at low values of P. In the right panel of Figure 1, depicting the radial variation of the length scales used in computing the turbulence-reduced drift coefficient, the quantities computed for a proton rigidity of 1 GV are indicated by solid lines, while the dashed lines represent those calculated for $P = 0.1$ GV. Note that for 1 GV protons, the turbulence-reduced and weak-scattering drift scales become comparable after a relatively small heliocentric distance, with the two quantities being indistinguishable beyond $\sim$2 au. For 0.1 GV protons, the turbulence reduction persists up to a greater radial distance of $\sim$10 au. It is therefore expected that if the effects of turbulence on particle drifts are taken into account, a Fisk-type signal in the computed CR intensities would most likely be seen for higher-rigidity protons farther away from the Sun.

In what follows, drift velocity profiles for both the Parker and SP hybrid fields will be compared, initially assuming a weak-scattering drift coefficient, in order to highlight the maximum effects due to the latter HMF model, and then employing a turbulence-reduced drift coefficient in order to investigate the resulting, potentially more realistic, ameliorated effects.

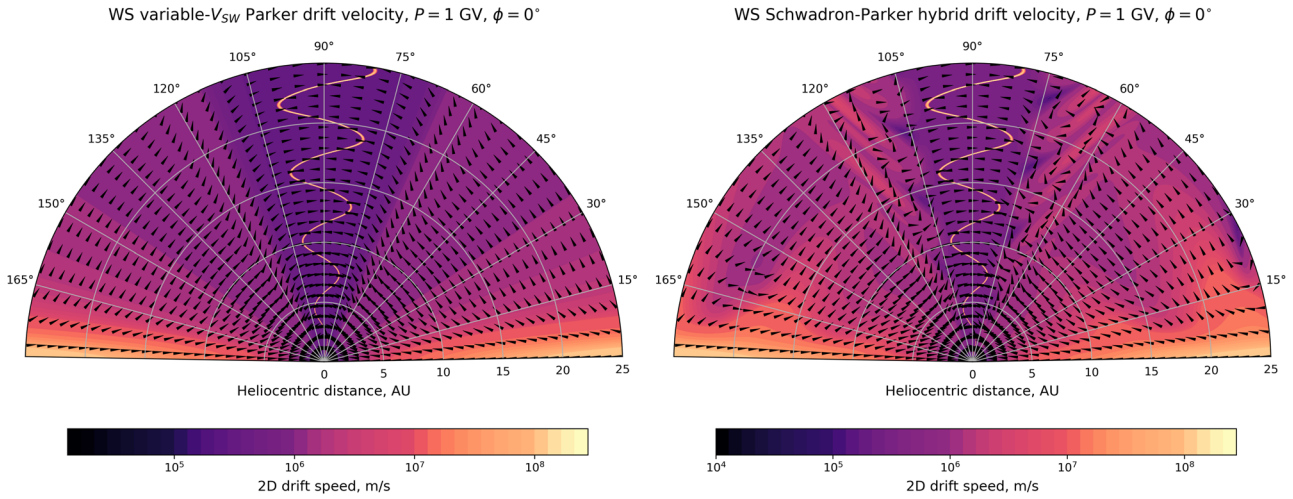

Figure 2. 2D drift velocity profiles calculated in the weak-scattering limit for the Parker HMF (with a latitude-dependent solar wind speed, shown on the left) and the SP hybrid HMF, shown on the right, for $A > 0$ conditions. A proton rigidity of 1 GV has been assumed.

2.1. Weak-scattering Drift Profiles

In Figure 2, the 2D drift velocity field (calculated from the radial and latitudinal components of $\vec{v}_d$) for 1 GV protons associated with the Parker HMF (with a latitude-dependent solar wind speed) is shown and compared with the corresponding drift velocity field as computed for the SP hybrid field of Hitge & Burger (2010). The drift velocity field computed for the Parker HMF is shown on the left, while the drift velocity associated with the SP hybrid HMF is shown on the right. The features seen for the Parker drift velocity are reminiscent of those presented by Jokipii & Thomas (1981), with two key differences: first, the 2D drift speed, calculated from the radial and latitudinal components of $\vec{v}_d$, is indicated in the figure, with brighter regions corresponding to higher drift speeds (whereas Jokipii & Thomas 1981 only show the drift trajectories). It is noted that the drift effects are strongest over the poles of the Sun and near the HCS. Second, because of the latitudinal dependence of V_{SW}, defined before, the direction of the overall drift velocity profile differs somewhat from what would be seen for a Parker field with a constant solar wind speed. In particular, the radial component of $\vec{v}_d$ is seen to be more significant at midlatitudes (e.g., near $\theta = 120°$), where the derivative of the solar wind speed is large. Except for such differences, the drift velocity profile of the Parker HMF is familiar: the drift is mostly latitudinal and, given $A > 0$ conditions, is directed from high latitudes toward the HCS. Along the HCS, protons drift outward, away from the Sun. Directly over the poles, protons drift toward the Sun. Given $A < 0$ conditions, all drift directions would be reversed.

The drift velocity profile of the SP hybrid HMF, shown in the right panel of Figure 2, differs from $\vec{v}_d$ as calculated for the Parker HMF in a number of regards. Such differences are most pronounced at midlatitudes, where the hybrid field of Hitge & Burger (2010) is most Fisk-like. In particular, it is noted that high-$|\vec{v}_d|$ structures extend from the polar regions (e.g., consider the structure found between 20 and 25 au from the Sun, between colatitudes of 0° and 45°). This feature results from the Fisk-like geometry of the HMF found at such regions (Troskie 2024). Furthermore, drift speeds are reduced in the regions found between the aforementioned high-speed structures (e.g., between 15 and 20 au from the Sun, from approximately 15°–45° colatitude). Changes in the direction of $\vec{v}_d$ are also clearly noted between the high-speed structures. Consider the direction of the drift velocity along the radial spoke at $\theta = 165°$: the drift is mostly latitudinal at the high-speed structures (e.g., around 17 au), while the radial component of $\vec{v}_d$ is more significant between the aforementioned structures (e.g., near 20 au). One of the most notable features of the SP hybrid drift velocity profile is a set of serrated structures found at colatitudes above and below the HCS (consider the structures seen between 60° and 75° as well as 105° and 120° colatitude). Enhancements in the drift speed are observed along such structures, and the direction of $\vec{v}_d$ is seen to be highly variable. These structures are unique to Schwadron-type fields, as they arise from the interplay between the latitude-dependent solar wind speed and the Fisk-like geometry of the hybrid HMF at such colatitudes (Troskie 2024). Over the poles and near the ecliptic plane, where the SP hybrid field reduces to the Parker HMF, it is seen that the drift effects are the same as those seen for a purely Parker field.

The drift effects discussed above are those arising from the geometries of the HMF models considered here. These effects, all of which are seen in the SP hybrid field, result from a combination of the effects observed for the Parker (1958) and Fisk (1996) HMF models and a latitude-dependent solar wind speed (e.g., McComas et al. 2003). However, some drift effects seen in Figure 2 result from the transition function (Burger & Hitge 2004; Burger et al. 2008) used in the Fisk–Parker and SP hybrid fields. For the latter field, these artificial drift effects include reduced-$|\vec{v}_d|$ regions, also associated with changes in the direction of $\vec{v}_d$, seen between the serrated structures found at midlatitudes. The drift effects arising from the transition function used in the hybrid Fisk-type fields are discussed in more detail in Troskie et al. (2023) and Troskie (2024).

In Figure 3, drift speed profiles (calculated from all three components of $\vec{v}_d$) computed for the SP hybrid HMF are shown. The different panels correspond to meridional projections of the drift speed profiles at different values of the azimuth: drift speeds calculated at 0° and 90° azimuth are shown in the left and right panels of the top row, respectively, while the bottom-row panels show $|\vec{v}_d|$ calculated at 180° and 270°. It is interesting to compare the 2D drift velocity profile of the SP hybrid HMF (right panel of Figure 2) to the corresponding 3D

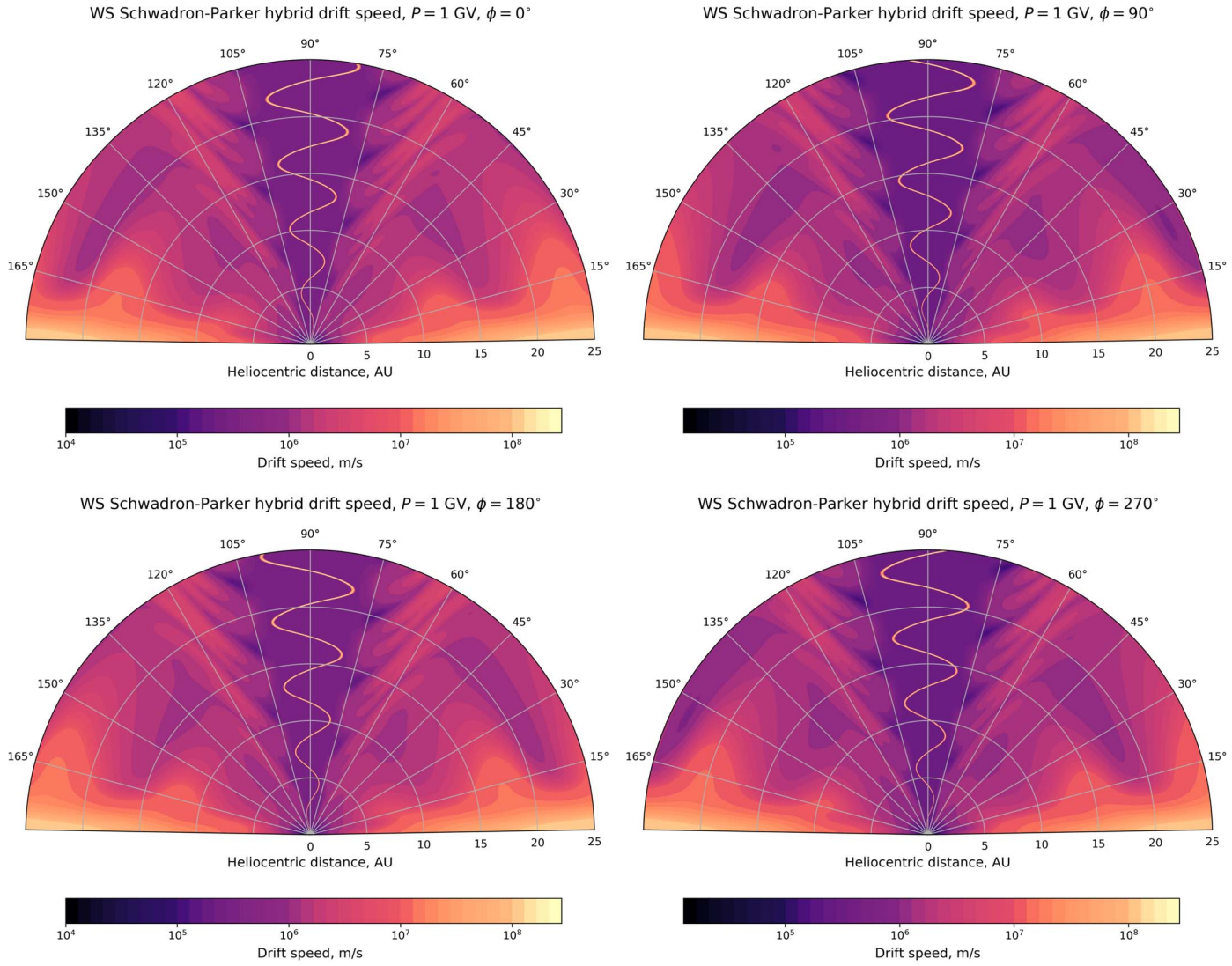

Figure 3. Weak-scattering drift speed profiles for the SP hybrid field, calculated from all components of $\vec{v}_d$, with a proton rigidity of 1 GV. The panels are shown at different values of the azimuth ϕ in order to illustrate the azimuthal dependence of certain drift effects seen for this HMF model, discussed in the text.

drift speed calculated at the same azimuth (the top left panel of Figure 3), as such a comparison highlights the effect of the azimuthal component of $\vec{v}_d$. In particular, it is seen, for example, that significant azimuthal drift occurs near the midlatitude serrations and the high-speed extensions over the poles, as these features are more prominent when the azimuthal drift velocity component is included in the calculation of $|\vec{v}_d|$.

Figure 3 also highlights the azimuthal variation of the drift effects calculated for the SP hybrid HMF. For example, consider the high-speed extension found between 15 and 20 au at $\phi = 0°$ (top left panel): as the value of ϕ increases, this structure is seen to decrease in size, with an azimuth-dependent reduction in its latitudinal extent as well as its width. This reduction occurs while the structure is seen to move closer to the Sun (with its heliocentric distance decreasing to under 15 au at an azimuth of 180°, shown in the bottom left panel). Therefore, were the drift velocity profile of the SP hybrid HMF to be considered in three dimensions, the structures appearing as high-speed extensions over the poles in 2D would be revealed to be cross sections of a large high-$|\vec{v}_d|$ structure spiraling from the Sun. The midlatitude serrations are similarly revealed to be 2D cross sections of 3D spiral structures: with an increase in the azimuth, a given serration will be seen to move closer to the Sun, and disappear at a sufficiently small heliocentric distance. Furthermore, a comparison of the (either left- or right-column) panels in the top and bottom rows of Figure 3 reveals that at a given azimuth ϕ_1, the drift velocity profile in the southern hemisphere is a reflection in the ecliptic plane of the drift velocity profile in the northern hemisphere at an azimuth $\phi_1 + 180°$.

2.2. Reducing Factors

Figure 4 shows turbulence-reduced drift velocity profiles calculated for the (latitude-dependent V_{SW}) Parker (left column) and SP hybrid (right column) HMF models. In the top row, a comparatively low proton rigidity of 0.1 GV has been assumed, resulting in few differences between the drift velocity profiles computed for the two HMF models; in the bottom row, for which a proton rigidity of 1 GV has been assumed, the differences between the Parker and SP hybrid drift velocity fields are more pronounced, as the turbulence-reduced drift scale calculated for this proton rigidity is comparable to the drift scale calculated in the weak-scattering limit. In the

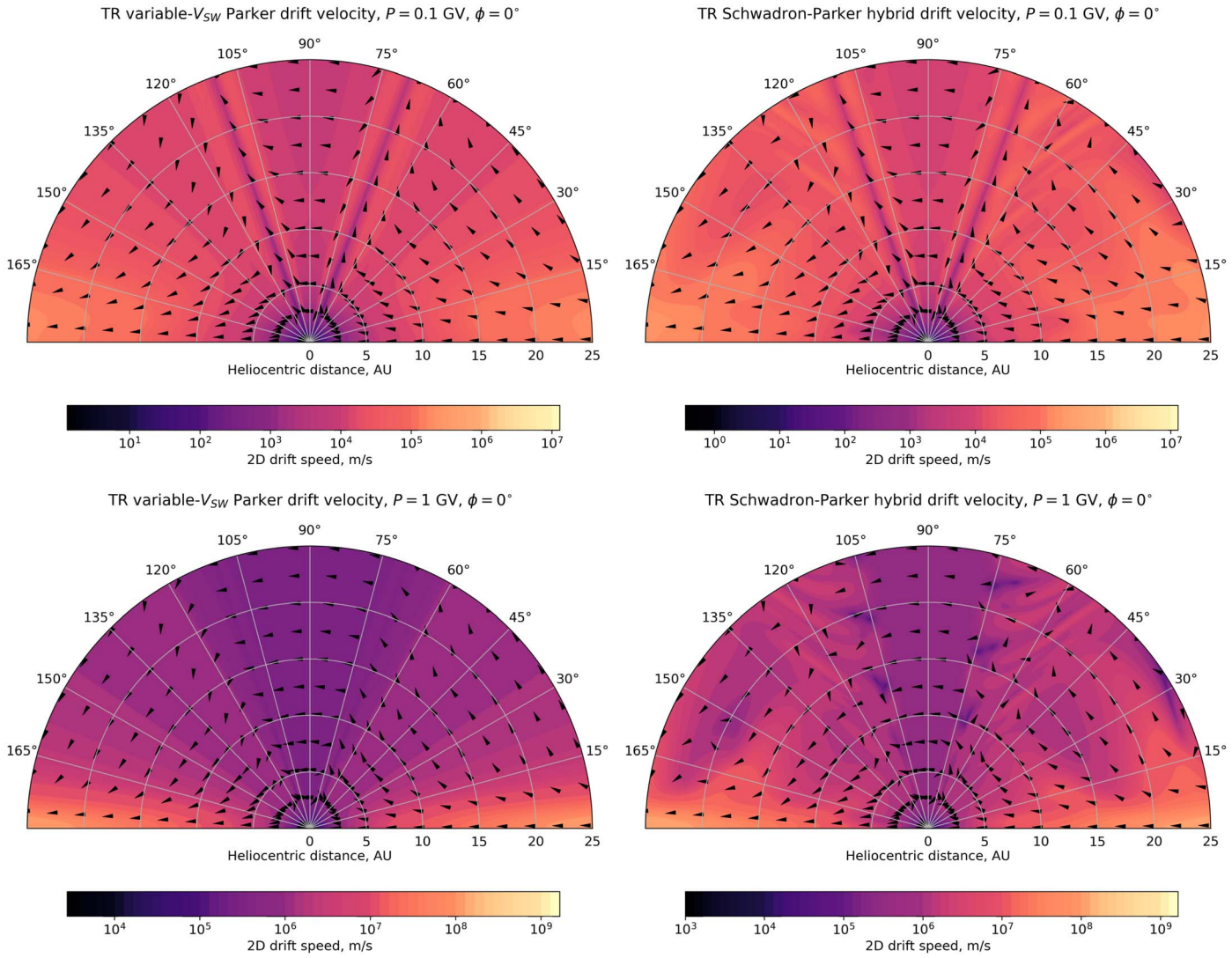

Figure 4. 2D turbulence-reduced drift velocity profiles computed for the Parker (with a latitude-dependent solar wind speed) and SP hybrid HMF models, shown in the left- and right-column panels, respectively. The panels shown in the top row have assumed a proton rigidity of 0.1 GV, while $P = 1$ GV for the bottom-row panels. In order to emphasize the effects of turbulence on gradient and curvature drift, the HCS has been removed.

(comparatively low-rigidity) drift velocity profiles shown in the top row, an especially prominent feature is a set of reduced-$|\vec{v}_d|$ radial spokes seen at colatitudes of approximately 70° and 110°, resulting from enhanced levels of turbulence due to stream-shear effects. Another feature seen in the drift velocity profiles of both fields at this rigidity is an especially significant reduction in the drift velocity over the poles: from directly over the poles to approximately 15° and 165° colatitude, the changes in $\vec{v}_d$ are much less pronounced than the changes observed across these colatitudes given a proton rigidity of 1 GV (bottom row), both with regard to the direction and the magnitude of $\vec{v}_d$. For $P = 0.1$ GV, some drift effects associated with the SP hybrid HMF remain: the enhancements to $|\vec{v}_d|$ at the midlatitude serrations discussed earlier, in the context of the weak-scattering drift velocity fields, are faintly visible, along with associated directional changes in $\vec{v}_d$.

3. CR Transport

Here, the influence of the drift effects discussed above on the computed GCR intensities and latitude gradients will be investigated in detail.

3.1. The Modulation Code

The present study employs the 3D, steady-state, stochastic solver introduced by Engelbrecht & Burger (2015a) of the Parker (1965) GCR transport equation:

$$\frac{\partial f}{\partial t} = \nabla \cdot (\boldsymbol{K} \cdot \nabla f) - \boldsymbol{V}_{sw} \cdot \nabla f + \frac{1}{3}(\nabla \cdot V_{sw}) \frac{\partial f}{\partial \ln p}, \quad (16)$$

where $f(\boldsymbol{r}, p, t) = p^{-2} j_T$ is the omnidirectional CR distribution function (Moraal 2013), incorporating both a standard Parker HMF, as well as a SP hybrid field, in order to calculate the GCR differential intensities j_T at Earth, as well as the latitude gradients of these particles. Elements of the diffusion tensor $\boldsymbol{K}$, which include diffusion coefficients parallel and perpendicular to the HMF, as well as the (turbulence-reduced) drift coefficient, are calculated as described in Section 2 (see Equation (14)), again employing inputs from the Oughton et al. (2011) turbulence transport model. The assumed solar wind

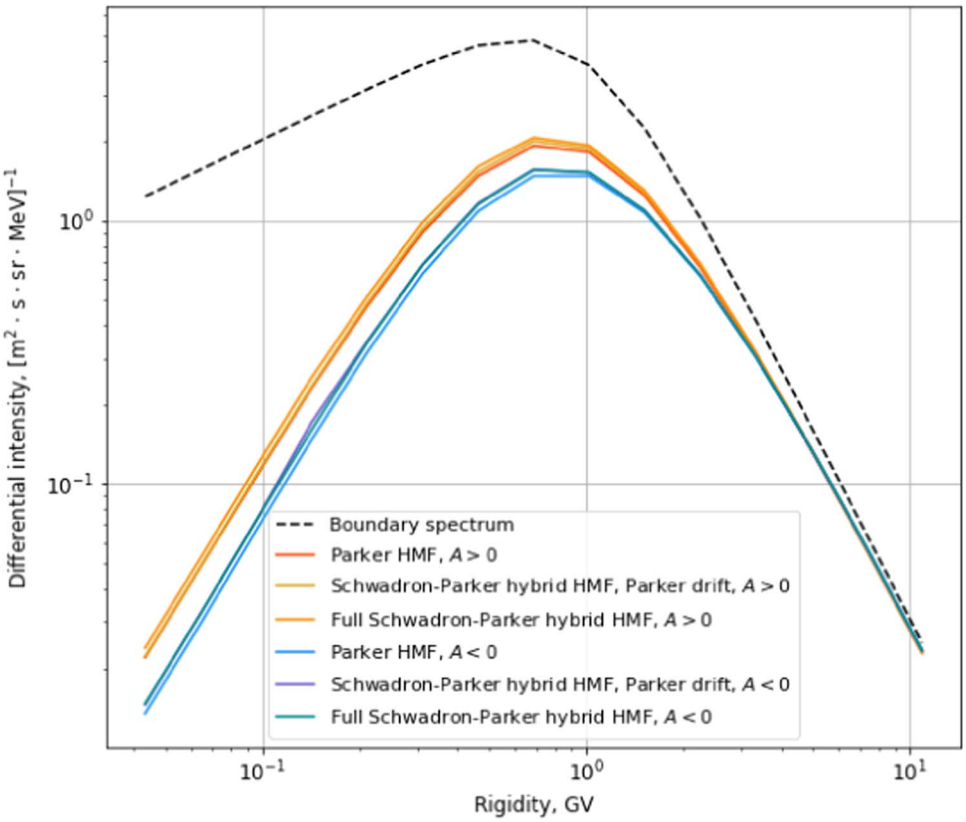

Figure 5. Differential intensities computed at Earth for GCR protons at different rigidities. Intensities are shown for $A > 0$ as well as $A < 0$ conditions, and were computed under the assumption of a Parker HMF (with a latitude-dependent solar wind speed), as well as the SP hybrid HMF, with and without appropriate drift effects. The Engelbrecht et al. (2019) HCS drift model has been implemented in all cases. The GCR boundary spectrum (Equation (17)) is also shown.

speed that enters into the terms describing the convection and adiabatic energy changes of the GCRs in Equation (16) is the the same as introduced in Section 2, as is the HCS latitudinal extent. For the sake of model consistency, a model boundary of 100 au is also assumed here. Therefore, as an input boundary differential intensity spectrum, we employ a fit to Voyager GCR proton observations near the termination shock proposed by Moloto et al. (2018), and given as function of particle rigidity P by

$$j_B^p = 17.0 \frac{(P/P_0)^{-2.4}}{2.2 + 2.1(P/P_0)^{-3.0}}, \tag{17}$$

in units of gigavolts, where $P_0 = 1$ GV. Although such an approach cannot fully take into account the considerable amount of modulation reported to occur in the heliosheath (e.g., Stone et al. 2013), it is nevertheless an improvement on simply using a full local interstellar spectrum. The GCR latitude gradients are calculated from the GCR proton differential intensities j_T computed with the abovementioned code, following the approach of Burger et al. (2008) and Engelbrecht & Burger (2010), such that

$$G_\theta(r) = \frac{\ln[\langle j_T(r, \theta_2, \phi)\rangle_\phi / \langle j_T(r, \theta_1, \phi)\rangle_\phi]}{\theta_1 - \theta_2}, \tag{18}$$

where $\theta_1 = 10°$ and $\theta_2 = 90°$ colatitude, with a radial distance of $r = 2$ au assumed in order to make qualitative comparisons with Ulysses observations of the same. Note that the angle brackets denote an azimuthal average of the differential intensities computed at a particular radial distance and colatitude. In order to calculate these azimuthal averages, differential intensities are calculated at 20 evenly spaced azimuthal angles for $N = 10{,}000$ pseudo-particles per energy bin, which would be appropriate for the calculation of G_θ (see the discussion of Moloto et al. 2019), and averaged accordingly. It should be noted that no attempt is made here to reproduce spacecraft observations and that only broad effects are investigated. As such, only qualitative comparisons with observations will be made.

3.2. GCR Intensities at Earth

Figure 5 shows the differential intensities for GCR protons computed at 1 au, at 90° colatitude and $\phi = 0°$, as a function of rigidity. Such intensities were calculated for the Parker (with a latitude-dependent solar wind speed) as well as the SP hybrid HMF model, with drift effects modeled assuming the Parker as well as the SP HMF geometry, respectively. The HCS drift model of Engelbrecht et al. (2019) has been implemented in all cases, and the boundary spectrum employed in this study (Equation (17)) is shown as a dashed black line. The intensities computed for $A > 0$ conditions are indicated by red or orange, while those calculated for $A < 0$ are shown as blue or purple, and seen to be lower than the $A > 0$ intensities across most of the present rigidity domain.

At 1 au in the ecliptic plane, few differences in the GCR intensities arising from the different HMF models are discernible. It is seen that the implementation of the SP hybrid HMF leads to a minor but definite increase in the GCR

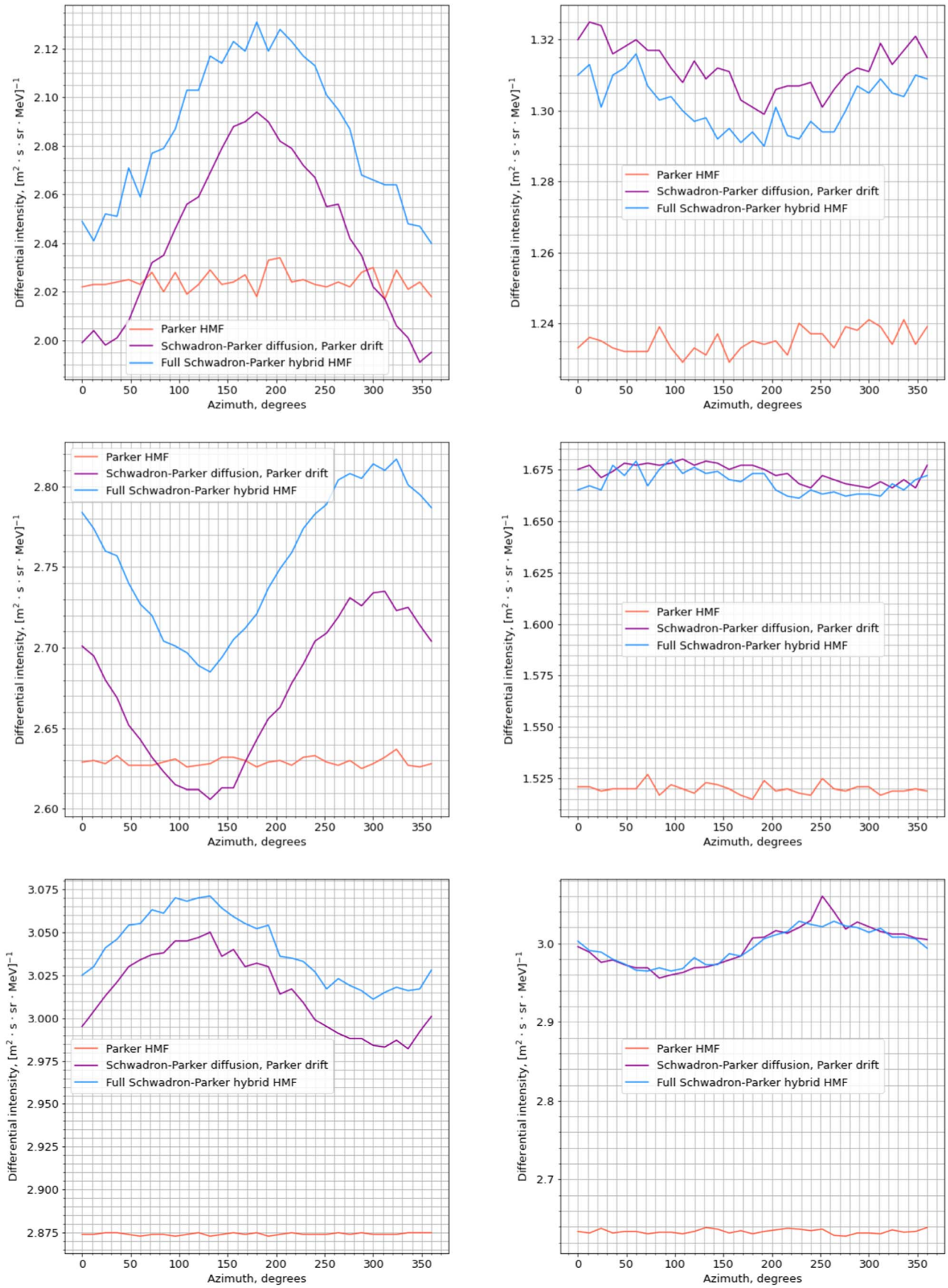

Figure 6. Differential intensities of 1 GV GCR protons, computed at 50° colatitude and different values of ϕ, for the Parker (red lines) and SP hybrid HMF models. For the latter model, the GCR intensities were computed with the combined effects of diffusion and drift taken into account (blue lines), as well as a combination of SP diffusion and Parker drift effects (purple lines). The left-column panels have assumed $A > 0$ conditions, while the figures shown in the right column were generated for $A < 0$ conditions. The different rows correspond to different heliocentric distances: 2, 10, and 50 au, from top to bottom.

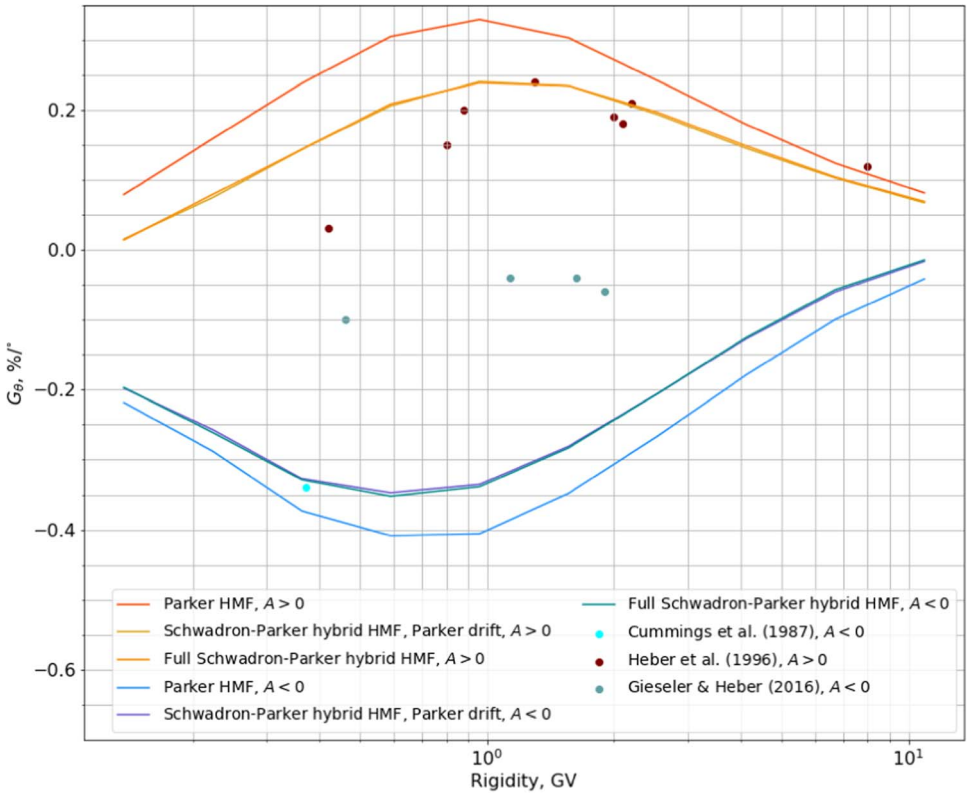

Figure 7. Latitude gradients calculated for both positive (red and orange) and negative (blue and purple) magnetic polarity conditions, as a function of rigidity, assuming a Parker or a SP HMF. Also shown are the observations reported by Cummings et al. (1987), Heber et al. (1996), and Gieseler & Heber (2016).

intensities (relative to those computed for a Parker field) across the rigidity domain under consideration, for $A > 0$ as well as $A < 0$. It is further noted that the SP hybrid drift velocity profile has a comparatively small effect on the computed GCR intensities, but that small differences can be discerned. For $A > 0$, it is seen that the GCR intensities computed for a combination of Parker drift effects and SP hybrid diffusion effects are higher than those calculated for the Parker HMF and lower than those computed for the full SP hybrid HMF (that is, with the hybrid field determining both drift and diffusion effects), especially near $P = 1$ GV. At lower rigidities, the inclusion of SP diffusion effects (in conjunction with the drift effects due to the Parker HMF) does not result in a discernible deviation from the GCR intensities computed for the Parker field. For $A < 0$, it is seen that the inclusion of SP diffusion effects results in an increase relative to the GCR intensities computed for a Parker field, while the implementation of a full SP hybrid field (that is, both diffusion and drift effects due to the SP hybrid HMF) results in GCR intensities more comparable to those computed for a combination of SP diffusion and Parker drift effects than to the intensities computed for a full Parker field.

3.3. Azimuthal GCR Intensity Variations

Figure 6 depicts the differential intensities computed for 1 GV GCR protons at different radial distances, as a function of azimuth ϕ. These intensities were computed at 50° colatitude for the Parker (red lines) as well as for the SP hybrid field, with the drifts calculated assuming a Parker field geometry (purple lines) and a full geometry (that is, including transport effects due to diffusion as well as drift effects calculated assuming a SP geometry; blue lines). The panels shown in the left and right columns correspond to positive and negative magnetic polarities, respectively, and the different rows correspond to different heliocentric distances (2, 10, and 50 au, from top to bottom).

As noted in the discussion of Figure 5, the implementation of the full SP hybrid HMF results in an increase in the GCR intensities relative to those computed assuming a Parker field, with a marked azimuthal variation, both for $A > 0$ and $A < 0$ conditions. A combination of SP diffusion and Parker drift effects results in the same variations, as can be seen when SP drift effects are taken into account, displaying only a relative decrease in intensities during $A > 0$. The Parker field leads to little or no azimuthal variation, as the fluctuations seen in the figure can be attributed to statistical variations resulting from the stochastic method used here to solve the Parker transport equation. As the radial distances increase, the form of the azimuthal variations resulting from the use of an SP field changes drastically, reflecting the azimuthal variations to be found in this HMF model. This is less evident for $A < 0$ conditions, as the drifts here are predominantly along the current sheet.

Relative amplitudes, as computed by Zhang (1997), are another measure of the effect of the SP hybrid HMF on GCR modulation. At 2 au, given $A > 0$ conditions, the relative amplitude computed for the SP hybrid HMF is 4%. It is interesting to note that these differences are reminiscent of the recurrent amplitudes reported as $6.1\% \pm 0.1\%$ from Ulysses data by Zhang (1997), although somewhat smaller.

3.4. Latitude Gradients

The computed GCR proton latitude gradients are shown as function of rigidity in Figure 7, alongside observations of the

same reported by Cummings et al. (1987), Heber et al. (1996), and Gieseler & Heber (2016), for both positive and negative magnetic polarity conditions. For $A > 0$, the latitude gradients calculated assuming a standard Parker HMF are close to those reported by Engelbrecht & Burger (2013) and Moloto et al. (2019), even though the diffusion coefficients employed here are different. Although somewhat larger than the observations, these computed G_θ remain comparable to them, due to the increased perpendicular diffusion coefficient at high latitudes, in turn a consequence of the higher turbulence levels over the poles as modeled here. For $A < 0$, G_θ computed for a pure Parker field is negative, but considerably larger in absolute value than the Gieseler & Heber (2016) observations, similar to what was reported by Engelbrecht & Burger (2013). The use of a SP hybrid field leads to latitude gradients reduced in absolute value relative to those computed assuming a Parker field for both magnetic polarities. While this brings G_θ closer to the Heber et al. (1996) observations during $A > 0$, this is not the case during $A < 0$. It is interesting to note, however, that the SP G_θ for $A < 0$ fall very close to the value for this quantity reported by Cummings et al. (1987) for solar cycle 22, given that the Gieseler & Heber (2016) observations were reported for the transition of solar cycle 23–24. The use of a Parker field drift velocity profile when employing a SP HMF does not greatly affect the computed latitude gradients.

4. Discussion and Conclusions

Not unexpectedly, a SP HMF leads to drift velocity profiles considerably different to those expected of a purely Parker field. A distinction, however, needs to be made. Globally, these profiles are similar, in the sense that both would, for positively charged particles, lead to drift velocities directed from high to low latitudes during periods of positive polarity, and vice versa during periods of negative polarity. Locally, however, SP drift velocity profiles display latitude- and azimuth-dependent whorls, with marked striations in the drift speed profiles, in regions where the SP field is more Schwadron-like. Such effects, of course, are ameliorated by the reducing influence of turbulence on drift.

The global similarities, but local differences, between the drift velocities calculated with the Parker and SP fields are reflected in their intensities at Earth calculated using a 3D, steady-state, ab initio GCR modulation code: regardless of magnetic polarity, 1 au GCR intensity spectra calculated employing a Parker field, a SP field with appropriate drift effects, or a SP field with Parker drift effects, display only small differences. This is a reflection of the global similarity of the drift velocity fields when turbulence-reduced drift coefficients are employed, as GCRs at 1 au have already experienced what is essentially an integrated sample of heliospheric conditions.

Local differences play a more significant role when azimuthal intensity variations at a fixed radial distance are considered. Here, the use of a SP field leads to GCR intensity variations not present when a Parker field is employed. While this is partly due to the azimuthal dependence of the SP field, and thus the resulting influence of this field geometry on the diffusion of the GCRs, a significant difference is noted between the azimuthal intensity variations computed using a SP field with SP-appropriate drifts versus those computed using a SP field with Parker-appropriate drifts, especially during $A > 0$ periods, with larger intensities computed for the former case. This reflects the local influence of the drifts on such variations. Intriguingly, the relative amplitudes at 2 au during $A > 0$ are qualitatively comparable to, though smaller than, the relative amplitude reported by Zhang (1997) for protons with rigidities larger than 0.426 GV.

Relative to the Parker field, the use of the SP field reduces the GCR proton latitude gradients computed at 2 au, as expected from previous studies (e.g., Burger & Hitge 2004; Burger et al. 2008; Hitge & Burger 2010). For $A > 0$, both fields yield results close to observations. However, for $A < 0$, this is not the case. This implies that another factor, related to charge-dependent effects, must be at play. Prior studies have been able to reproduce the observed $A < 0$ latitude gradients, using models that assume anisotropic perpendicular diffusion (e.g., Burger et al. 2000; Shen et al. 2021). Such an assumption, however, would not explain the charge-sign-dependent discrepancy reported on here. It is interesting to note that the cited studies employ different forms for the drift coefficient reduction factor. However, Shen et al. (2021) employ a factor dependent on turbulence, via the magnetic variance differing only somewhat from the result of Engelbrecht et al. (2017), but assume that magnetic variances at high latitudes are smaller than those at low latitudes (for a given radial distance). From Ulysses observations, this is not the case (see, e.g., Forsyth et al. 1996; Bavassano et al. 2000a, 2000b; Erdős & Balogh 2005). Last, although a solar cycle dependence for latitude gradients is not expected (see, e.g., Munakata et al. 1999; Morales-Olivares & Caballero-Lopez 2010), it is known that there can be considerable variation in GCR transport parameters from one solar minimum/maximum to the next, due to inherent differences in the large- and small-scale heliospheric plasma parameters they depend upon (e.g., Duggal et al. 1983; Storini et al. 1995; de Toma et al. 2010; Zhao et al. 2018; Caballero-Lopez et al. 2019; Li et al. 2021; Burger et al. 2022), which can have a considerable influence on the GCR intensities (see Moloto et al. 2018; Engelbrecht & Wolmarans 2020). These factors may also influence the computed latitude gradients and may need to be taken into account when comparisons with observations taken during different solar minima, such as those shown in Figure 7, are made. Such a comparison, alongside a study of the influence of anisotropic perpendicular diffusion, will be the subject of future work.

Acknowledgments

This work is based on research supported in part by the National Research Foundation of South Africa (NRF grant Nos. 137793, 142146, and TTK2204183656). The opinions expressed and conclusions arrived at are those of the authors and are not necessarily to be attributed to the NRF. The responsibility for the contents of this work is with the authors. The authors would like to thank K.D. Moloto for useful discussions on GCR modulation.

Software: Matplotlib (Hunter 2007), NumPy (Harris et al. 2020).

ORCID iDs

J. S. Troskie https://orcid.org/0000-0002-6242-7056
N. E. Engelbrecht https://orcid.org/0000-0003-3659-7956
P. J. Steyn https://orcid.org/0000-0003-2099-8093

References

Adhikari, L., Zank, G. P., & Zhao, L. 2021, Fluids, 6, 368
Bavassano, B., Pietropaolo, E., & Bruno, R. 2000a, JGR, 105, 12697
Bavassano, B., Pietropaolo, E., & Bruno, R. 2000b, JGR, 105, 15959
Burger, R. A. 2012, ApJ, 760, 60
Burger, R. A., & Hitge, M. 2004, ApJL, 617, L73
Burger, R. A., Krüger, T. P. J., Hitge, M., & Engelbrecht, N. E. 2008, ApJ, 674, 511
Burger, R. A., Moraal, H., & Webb, G. M. 1985, Ap&SS, 116, 107
Burger, R. A., Nel, A. E., & Engelbrecht, N. E. 2022, ApJ, 926, 128
Burger, R. A., Potgieter, M. S., & Heber, B. 2000, JGR, 105, 27447
Burger, R. A., & Sello, P. C. 2005, AdSpR, 35, 643
Caballero-Lopez, R. A., Engelbrecht, N. E., & Richardson, J. D. 2019, ApJ, 883, 73
Cummings, A. C., Stone, E. C., & Webber, W. R. 1987, GeoRL, 14, 174
de Simone, N., di Felice, V., Gieseler, J., et al. 2011, ASTRA, 7, 425
de Toma, G., Gibson, S., Emery, B., & Kozyra, J. 2010, in AIP Conf. Ser. 1216, 12th International Solar Wind Conference, ed. M. Maksimovic et al. (Melville, NY: AIP), 667
Duggal, S. P., Pomerantz, M. A., Schaefer, R. K., & Tsao, C. H. 1983, JGR, 88, 2973
Ebert, D. S., Musgrave, F. K., Peachey, D., Perlin, K., & Worley, S. 2002, Texturing and Modeling: A Procedural Approach (3rd edn.; San Francisco, CA: Morgan Kaufmann Publishers Inc.)
Engelbrecht, N., & Burger, R. 2015a, ApJ, 814, 152
Engelbrecht, N. E. 2017, ApJL, 849, L15
Engelbrecht, N. E., & Burger, R. A. 2010, AdSpR, 45, 1015
Engelbrecht, N. E., & Burger, R. A. 2013, ApJ, 772, 46
Engelbrecht, N. E., & Burger, R. A. 2015b, AdSpR, 55, 390
Engelbrecht, N. E., Mohlolo, S. T., & Ferreira, S. E. S. 2019, ApJL, 884, L54
Engelbrecht, N. E., & Moloto, K. D. 2021, ApJ, 908, 167
Engelbrecht, N. E., Strauss, R. D., le Roux, J. A., & Burger, R. A. 2017, ApJ, 841, 107
Engelbrecht, N. E., & Wolmarans, C. P. 2020, AdSpR, 66, 2722
Engelbrecht, N. E., Effenberger, F., Florinski, V., et al. 2022, SSRv, 218, 33
Erdős, G., & Balogh, A. 2005, AdSpR, 35, 625
Ferreira, S. E. S., Potgieter, M. S., Burger, R. A., Heber, B., & Fichtner, H. 2001, JGR, 106, 24979
Fisk, L. A. 1996, JGR, 101, 15547
Fisk, L. A. 2001, JGR, 106, 15849
Forman, M. A., Jokipii, J. R., & Owens, A. J. 1974, ApJ, 192, 535
Forsyth, R. J., Balogh, A., & Smith, E. J. 2002, JGRA, 107, 1405
Forsyth, R. J., Horbury, T. S., Balogh, A., & Smith, E. J. 1996, GeoRL, 23, 595
Fraternale, F., Adhikari, L., Fichtner, H., et al. 2022, SSRv, 218, 50
Gieseler, J., & Heber, B. 2016, A&A, 589, A32
Gosling, J. T., & Pizzo, V. J. 1999, in Corotating Interaction Regions. Series: Space Sciences Series of ISSI, ed. A. Balogh et al., 7 (Dordrecht: Springer), 21
Harris, C. R., Millman, K. J., van der Walt, S. J., et al. 2020, Natur, 585, 357
Heber, B., Dröge, W., Kunow, H., et al. 1996, GeoRL, 23, 1513
Heber, B., Gieseler, J., Dunzlaff, P., et al. 2008, ApJ, 689, 1443
Hitge, M., & Burger, R. A. 2010, AdSpR, 45, 18
Hunter, J. D. 2007, CSE, 9, 90
Isenberg, P. A., & Jokipii, J. R. 1979, ApJ, 234, 746
Jokipii, J. R. 1966, ApJ, 146, 480
Jokipii, J. R. 1973, ApJ, 182, 585
Jokipii, J. R., Kóta, J., Giacalone, J., Horbury, T. S., & Smith, E. J. 1995, GeoRL, 22, 3385
Jokipii, J. R., & Thomas, B. 1981, ApJ, 243, 1115
Kobylinski, Z. 2001, AdSpR, 27, 541
Kopp, A., Wiengarten, T., Fichtner, H., et al. 2017, ApJ, 837, 37
Kóta, J., & Jokipii, J. R. 1983, ApJ, 265, 573
Kóta, J., & Jokipii, J. R. 1998, SSRv, 83, 137
Li, H., Feng, X., & Wei, F. 2021, ApJL, 917, L26
Lionello, R., Linker, J. A., Mikić, Z., & Riley, P. 2006, ApJL, 642, L69
Matthaeus, W. H., Qin, G., Bieber, J. W., & Zank, G. P. 2003, ApJL, 590, L53
McComas, D. J., Elliott, H. A., Schwadron, N. A., et al. 2003, GeoRL, 30, 1517
McComas, D. J., Barraclough, B. L., Funsten, H. O., et al. 2000, JGR, 105, 10419
Mohlolo, S. T., Engelbrecht, N. E., & Ferreira, S. E. S. 2022, AdSpR, 69, 2574
Moloto, K. D., Engelbrecht, N. E., & Burger, R. A. 2018, ApJ, 859, 107
Moloto, K. D., Engelbrecht, N. E., Strauss, R. D., Moeketsi, D. M., & van den Berg, J. P. 2019, AdSpR, 63, 626
Moraal, H. 2013, SSRv, 176, 299
Morales-Olivares, O. G., & Caballero-Lopez, R. A. 2010, AdSpR, 46, 1313
Munakata, K., Sakurai, I., Miyasaka, H., et al. 1999, AdSpR, 23, 459
Ness, N. F., & Burlaga, L. F. 2001, JGR, 106, 15803
Neugebauer, M. 1976, JGR, 81, 78
Oughton, S., & Engelbrecht, N. E. 2021, NewA, 83, 101507
Oughton, S., Matthaeus, W. H., Smith, C. W., Breech, B., & Isenberg, P. A. 2011, JGRA, 116, A08105
Paizis, C., Heber, B., Ferrando, P., et al. 1999, JGR, 104, 28241
Palmer, I. D. 1982, RvGeo, 20, 335
Parker, E. N. 1958, ApJ, 128, 664
Parker, E. N. 1965, P&SS, 13, 9
Phillips, J. L., Bame, S. J., Barnes, A., et al. 1995, GeoRL, 22, 3301
Roberts, D. A., Giacalone, J., Jokipii, J. R., Goldstein, M. L., & Zepp, T. D. 2007, JGRA, 112, A08103
Schwadron, N. A. 2002, GeoRL, 29, 1663
Schwadron, N. A., & McComas, D. J. 2003, GeoRL, 30, 1587
Shalchi, A. 2009, Nonlinear Cosmic Ray Diffusion Theories, Astrophysics and Space Science Library, Vol. 362 (Berlin: Springer)
Shalchi, A., Bieber, J. W., & Matthaeus, W. H. 2004, ApJ, 604, 675
Shen, Z., Qin, G., Zuo, P., Wei, F., & Xu, X. 2021, ApJS, 256, 18
Simpson, J. A., Connell, J. J., Lopate, C., McKibben, R. B., & Zhang, M. 1995a, GeoRL, 22, 3337
Simpson, J. A., Anglin, J. D., Bothmer, V., et al. 1995b, Sci, 268, 1019
Smith, C. W., & Bieber, J. W. 1991, ApJ, 370, 435
Snodgrass, H. B. 1983, ApJ, 270, 288
Sternal, O., Engelbrecht, N. E., Burger, R. A., et al. 2011, ApJ, 741, 23
Steyn, P. J., & Burger, R. A. 2020, ApJ, 902, 33
Steyn, P. J., Johnson, D., Botha, G. J. J., & Régnier, S. 2024, ApJ, 966, 77
Stone, E. C., Cummings, A. C., McDonald, F. B., et al. 2013, Sci, 341, 150
Storini, M., Borello-Filisetti, O., Mussino, V., Parisi, M., & Sykora, J. 1995, SoPh, 157, 375
Strauss, R. D., Potgieter, M. S., Büsching, I., & Kopp, A. 2012, Ap&SS, 339, 223
Teufel, A., & Schlickeiser, R. 2003, A&A, 397, 15
Troskie, J. S., Engelbrecht, N. E., & Steyn, P. J. 2023, in Proc. 67th Annual Conf. of the South African Institute of Physics (SAIP), 1 (Pretoria: SAIP), 341
Troskie, J. S. 2024, Modelling galactic cosmic ray drifts in the presence of a Fisk-type heliospheric magnetic field, Master's thesis, North-West Univ. (Potchefstroom campus)
Wenzel, K. P. 1995, NuPhS, 39, 59
Wenzel, K. P., Marsden, G. R., Page, E. D., & Smith, J. E. 1990, ICRC (Adelaide), 21, 252
Williams, L. L., & Zank, G. P. 1994, JGR, 99, 19229
Zhang, M. 1997, ApJ, 488, 841
Zhao, L. L., Adhikari, L., Zank, G. P., Hu, Q., & Feng, X. S. 2018, ApJ, 856, 94
Zurbuchen, T. H., Schwadron, N. A., & Fisk, L. A. 1997, JGR, 102, 24175